RESEARCH ARTICLE

# Optimizing Potassium Sodium Niobate Content in PVDF Composite Films for Enhanced $\beta$-Phase Crystallization, Ferroelectric Hysteresis, and Energy Storage Performance

**Numan Ali**[1], **Khizar Hayat**[1,*], **Muhammad Uzair**[1], **Aisha Khattak**[1] and **Said Karim Shah**[1,*]

[1] Department of Physics, Abdul Wali Khan University Mardan, Mardan 23200, Khyber Pakhtunkhwa, Pakistan

## Abstract

**Lead-free polymer-ceramic composites that combine the flexibility of poly(vinylidene fluoride) (PVDF) with the strong polarization of ferroelectric ceramic fillers are candidates for flexible energy-storage devices. In this work, PVDF/potassium sodium niobate ($K_{0.5}Na_{0.5}NbO_3$, KNN) composite films were prepared by solvent casting. The KNN loading was varied from 0.1 to 0.5 g at a fixed PVDF content of 0.5 g, and a 3 kV DC voltage was applied during drying. X-ray diffraction and Fourier-transform infrared spectroscopy showed that the electroactive $\beta$-phase of PVDF coexists with the perovskite KNN phase; the $\beta$-phase fraction reached a maximum of 83.7% at a PVDF:KNN mass ratio of 0.5:0.4. Polarization-electric field ($P$-$E$) loops measured between 100 and 350 kV cm$^{-1}$ showed that this composition gave the highest maximum polarization ($P_{max}$ = 0.321 $\mu$C cm$^{-2}$) and the largest polarization difference ($\Delta P$ = 0.211 $\mu$C cm$^{-2}$). At 350 kV cm$^{-1}$ it delivered a recoverable energy density ($U_{rec}$) of 0.0154 J cm$^{-3}$, an efficiency ($\eta$) of 36.05%, and a total energy density ($U_T$) of ≈0.043 J cm$^{-3}$. Field-emission scanning electron microscopy showed a rougher, more heterogeneous surface after KNN addition, consistent with filler dispersion in the PVDF matrix. Within this series, the 0.5:0.4 composition offers the best balance between polarization and stored energy. The absolute energy densities remain low because the films were tested only up to 350 kV cm$^{-1}$; higher-field testing is required before PVDF/KNN films can be judged against other lead-free dielectric composites.**

**Keywords**: PVDF, potassium sodium niobate (KNN), $\beta$-phase, ferroelectric composite, polarization-electric field hysteresis, energy storage density.

## 1 Introduction

Polymer-based composite films with good mechanical and dielectric properties are widely studied for flexible energy-storage and dielectric devices [1]. Among

**Submitted:** 29 September 2026
**Revised:** 23 October 2026
**Accepted:** 24 October 2026
**Published:** 20 November 2026

**Vol.** 2, **No.** 4, 2026.
10.62762/JAEM.2026.500870

***Corresponding author:**
✉ Khizar Hayat
khizarhayat@awkum.edu.pk
✉ Said Karim Shah
saidkarim@awkum.edu.pk

**Citation**
Ali, N., Hayat, K., Uzair, M., Khattak, A., & Shah, S. K. (2026). Optimizing Potassium Sodium Niobate Content in PVDF Composite Films for Enhanced $\beta$-Phase Crystallization, Ferroelectric Hysteresis, and Energy Storage Performance. *Journal of Advanced Electronic Materials*, 2(4), 120–136.

© 2026 by the Authors. Published by Institute of Central Computation and Knowledge. This is an open access article under the CC BY license (https://creativecommons.org/licenses/by/4.0/).

the available polymers, poly(vinylidene fluoride) (PVDF) has received the most attention because of its ferroelectric, piezoelectric, pyroelectric and dielectric properties [2, 3]. It is also flexible, easy to process and thermally stable [4]. PVDF can crystallize in several polymorphs ($\alpha$, $\beta$, $\gamma$, $\delta$ and $\varepsilon$), but its electroactive response is dominated by the polar all-trans $\beta$-phase [5], so raising the $\beta$-phase content is a direct way to improve ferroelectric and energy-storage performance. Under ordinary processing conditions, PVDF crystallizes mainly in the non-polar $\alpha$-phase, and the $\beta$-phase usually forms only under an external stimulus such as stretching or a strong poling field. Fillers have also been used to nucleate the electroactive phases, including ceramic nanoparticles [6, 7], ZnO [8, 9], carbon nanotubes [10], clay [11], and boron nitride and reduced graphene oxide [12]. The large filler loadings often needed for a high $\beta$-phase fraction, however, reduce the flexibility of PVDF and limit its use in flexible and wearable devices [13]. The $\beta$-phase content has also been raised by mechanical stretching, electric poling and thermal annealing [13, 14, 17]; these treatments align the chains and convert the $\alpha$-phase into the $\beta$-phase. Structural modification of PVDF-based ferroelectric polymers, for example relaxor-like ferroelectric polymers and extended-chain polymers containing relaxor-like secondary crystals, has also been used to obtain large electromechanical responses [15, 16].

Ceramic capacitors are also widely studied for electrical energy storage because of their thermal stability, high power density and fast charge-discharge response [18–20]. Their $P$-$E$ behaviour is commonly tuned by compositional engineering, such as doping, ionic substitution or solid-solution formation, which refines the grains and suppresses grain-boundary diffusion. For example, Yang et al. showed that adding $BiFeO_3$ to $K_{0.5}Na_{0.5}NbO_3$ reduced the grain size from 5.4 to 0.15 $\mu$m and gave $U_{rec} = 2\ J\,cm^{-3}$ at 206 kV cm$^{-1}$ in $0.9K_{0.5}Na_{0.5}NbO_3$-$0.1BiFeO_3$ ceramics [21]. Another approach relies on polar nano-regions (PNRs), which switch over lower energy barriers than macroscopic domains. Ceramics dominated by PNRs therefore show slim $P$-$E$ loops with high $U_{rec}$ and efficiency. Using a nanoscale polarization-mismatch strategy, Hu et al. [22] obtained $U_{rec} = 4.49\ J\,cm^{-3}$ at 93% efficiency in $0.6BaTiO_3$-$0.4Bi(Mg_{1/2}Ti_{1/2})O_3$ ceramics.

Ceramic capacitors, however, are brittle, inflexible and difficult to process [23, 24], which rules them out for flexible devices. In addition, their relatively high remnant polarization ($P_r$) lowers the recoverable energy, and their breakdown strength is limited by porosity and grain-boundary defects. For a linear dielectric capacitor, the stored energy density ($U$) is given by Eq. (1), which makes the breakdown strength the key parameter for polymer film capacitors [25]:

$$U = \frac{1}{2}\varepsilon_0\varepsilon_r E_b^2 \tag{1}$$

where $\varepsilon_0$ is the vacuum permittivity, $\varepsilon_r$ is the relative permittivity and $E_b$ is the breakdown strength. Eq. (1) follows from $U = \int_0^{E_b} E\,\mathrm{d}D$ with $D = \varepsilon_0\varepsilon_r E$, and is therefore the maximum energy density of a *linear* dielectric. For nonlinear, hysteretic materials such as the films studied here, the energy densities must instead be obtained by integrating the measured $P$-$E$ loops (Eqs. (3)-(5)); because $\varepsilon_r \gg 1$, $D \approx P$.

Polymer-ceramic composites have been widely explored to overcome the brittleness of ceramics while keeping useful dielectric properties [26]. Ceramic fillers usually have a high $\varepsilon_r$ but a low $E_b$, whereas polymers combine a lower $\varepsilon_r$ with a much higher $E_b$ [26, 27].

Lead-free perovskite $ABO_3$ ceramics are dielectrics with strong polarization that are widely studied for energy storage [28]. They are also common fillers in PVDF composites, where their strong polarization raises both the $\beta$-phase content of PVDF and the dielectric response of the composite [24, 27]. Their ferroelectric nature, however, also brings a sizeable $P_r$, which increases hysteresis loss during charge-discharge cycling and limits the usable energy density. Good energy storage therefore requires a high $P_{max}$, a low $P_r$ and a high $E_b$ at the same time.

PVDF-ceramic composites thus combine the processability and flexibility of PVDF with the functional response of the filler, and the filler can also promote $\beta$-phase formation. Potassium sodium niobate ($K_{0.5}Na_{0.5}NbO_3$, KNN) is attractive as a lead-free, environmentally benign ferroelectric filler with favourable polarization characteristics [24, 27].

In this study, PVDF/KNN composite films were prepared by solvent casting, and their $\beta$-phase content and ferroelectric response were examined for flexible energy storage. The KNN loading was varied to find the composition that gives a high $P_{max}$ with a low $P_r$. All films were dried under the same 3 kV DC voltage; the effect of the KNN content on the $\beta$-phase fraction, the $P$-$E$ response and the energy-storage parameters is reported.

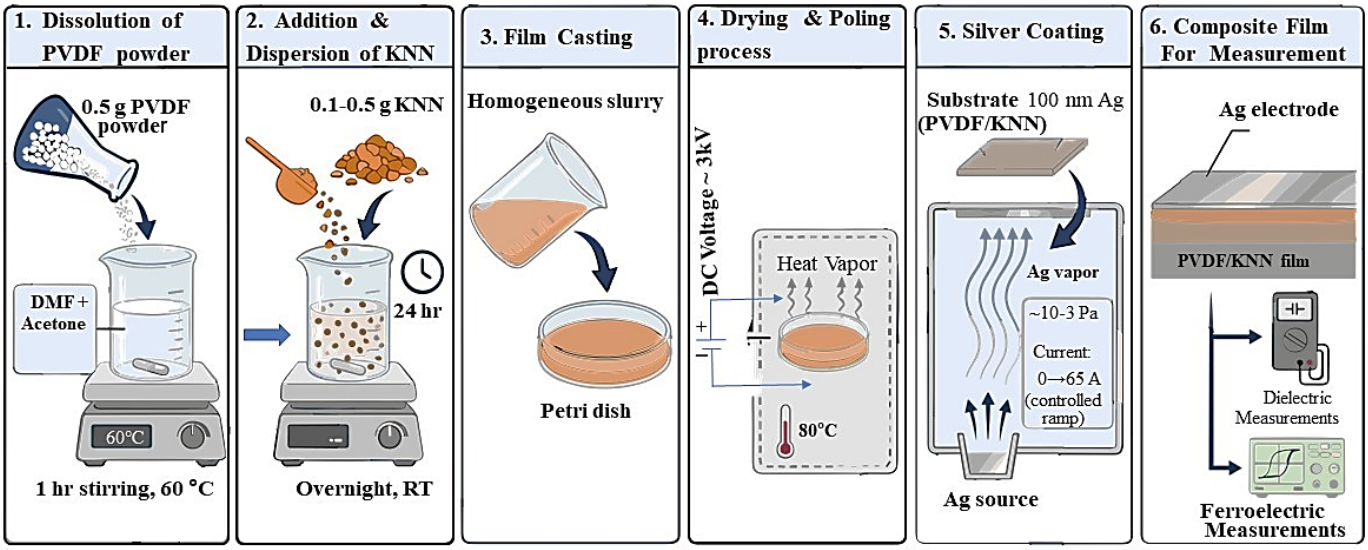



**Figure 1.** Preparation of PVDF/KNN composite films by solvent casting.

## 2 Materials, synthesis and experimental procedures

### 2.1 Materials

Potassium carbonate ($K_2CO_3$, 99.9%), sodium carbonate ($Na_2CO_3$, 99.9%), niobium pentoxide ($Nb_2O_5$, 99.8%), PVDF (-$(C_2H_2F_2)_n$-, analytical grade, $M_w$ = 1 200 000 g mol$^{-1}$), *N*,*N*-dimethylformamide (DMF, anhydrous, 99.8%) and acetone (ACS reagent, ≥99.5%) were purchased from Sigma-Aldrich and used as received.

### 2.2 Synthesis of KNN particles

KNN powder was synthesized by the conventional solid-state (mixed-oxide) route. $K_2CO_3$, $Na_2CO_3$ and $Nb_2O_5$ were first dried at 200 °C for several hours to remove absorbed moisture and organic residues. The precursors were weighed in stoichiometric ratio and ball-milled for 24 h in a polyethylene jar with $Y_2O_3$-stabilized $ZrO_2$ media and ethanol as the dispersing medium; good mixing at this stage is needed for complete formation of $K_{0.5}Na_{0.5}NbO_3$ during calcination. The slurry was sieved and dried overnight at 100 °C. The dried powder was ground in an agate mortar and passed through a 180 $\mu$m mesh, and then calcined at 1000 °C for 11 h at a heating rate of 5 °C min$^{-1}$. The calcined powder was reground and sieved to obtain fine KNN particles for the PVDF solution. The synthesis route is shown in Figure S1.

### 2.3 Synthesis of PVDF/KNN composite films

PVDF and PVDF/KNN composite films were prepared by solvent casting (Figure 1). The PVDF content was fixed at 0.5 g and the KNN content was 0.1-0.5 g. PVDF was dissolved in a DMF/acetone mixture under magnetic stirring on a hot plate for 1 h to obtain a homogeneous solution with a viscosity suitable for casting. The KNN powder was then added gradually and the mixture was stirred overnight at room temperature. The slurry was cast into a Petri dish, which was placed between two metal plates separated by 5 cm inside a vacuum oven at 80 °C. A DC voltage of 3 kV was applied across the plates during drying to promote dipole alignment and reduce residual porosity. Silver electrodes (≈100 nm thick) were then deposited on both film surfaces by thermal evaporation under high vacuum (≈$10^{-3}$ Pa), raising the deposition current gradually from 0 to 65 A. Photographs of the films are given in Figure S2.

### 2.4 Characterization techniques

The phase composition of the PVDF and PVDF/KNN films was examined by X-ray diffraction (XRD; JEOL JDX-3532, Japan; Cu K$\alpha$ radiation, $\lambda$ = 1.5418 Å). Phase evolution was further examined by Fourier-transform infrared spectroscopy (FTIR; PerkinElmer Spectrum Two). The morphology of the KNN particles and of the films was observed by field-emission scanning electron microscopy (FE-SEM; TESCAN MAIA3). *P*-*E* hysteresis loops were recorded with a ferroelectric test system (PolyK Technologies, State College, PA, USA).

## 3 Results and discussion

### 3.1 Structural analysis (XRD)

Figure 2(a) shows the XRD pattern of the pure PVDF film. The peak near 2$\theta$ ≈ 20.3° is assigned to the polar

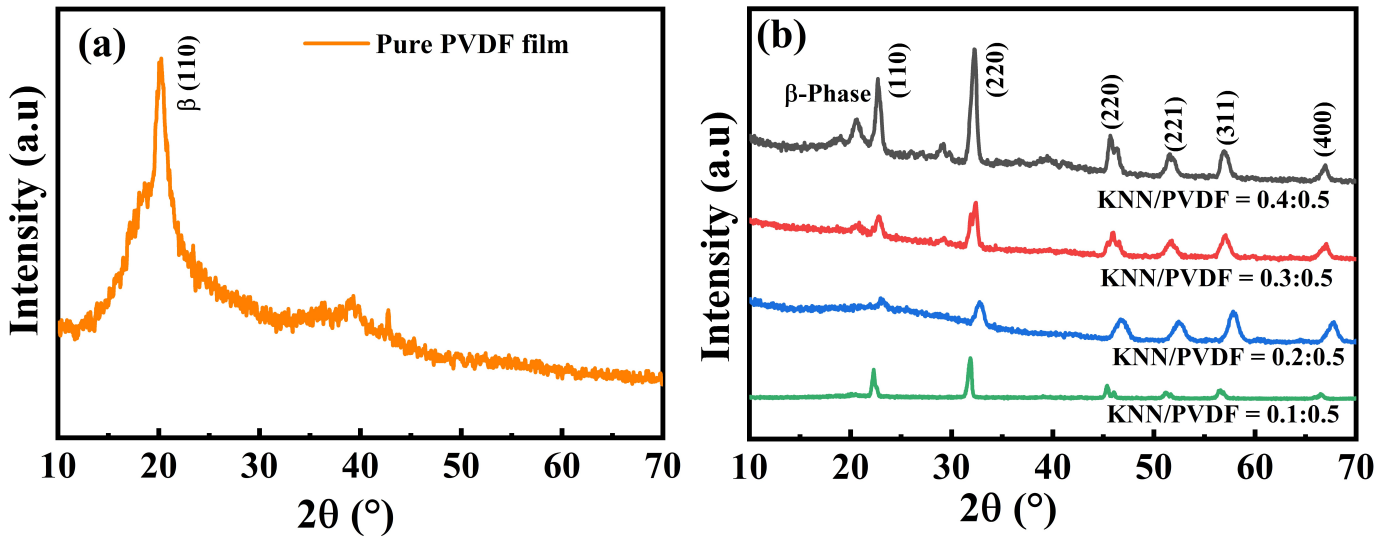



**Figure 2.** XRD patterns of (a) pure PVDF and (b) PVDF/KNN composite films dried at 80 °C under a 3 kV DC voltage.

$\beta$-phase [3, 24, 29], and its broad profile reflects the semi-crystalline nature of the polymer. Because the $\alpha$(110) reflection (20.0°) lies close to this position and a shoulder near 18.4° is visible, the XRD assignment is supported by the FTIR results in Section 3.3. The XRD pattern of the synthesized KNN powder, whose average size is about 9.12 $\mu$m, is shown in Figure S3. Figure 2(b) shows the patterns of the composite films with 0.1-0.4 g KNN. The $\beta$-phase peak near 20.3° is clearly resolved for the 0.3 and 0.4 g films and is most intense at a PVDF:KNN mass ratio of 0.5:0.4, whereas it is weak or not resolved at 0.1 and 0.2 g, where it is probably masked by the broad amorphous background; the FTIR results (Section 3.3) nevertheless give $\beta$-phase fractions of 68% and 74.1% for these two films. Sharper reflections at higher angles are indexed to the (110), (200), (220), (221), (311) and (400) planes of perovskite KNN. The weaker peak at low loadings suggests that a sufficient KNN content is needed to drive the conformational change of PVDF towards the $\beta$-phase. A slight change in peak shape around 20.3° may come from overlap with the low-angle tail of the KNN reflection near 22°. The distinct KNN reflections together with the retained $\beta$-phase peak confirm that KNN was incorporated without destroying the polymer structure. Such coexistence is expected to favour interfacial coupling between PVDF and KNN.

### 3.2 Morphological analysis (FE-SEM)

Figures 3(a) and 3(b) show FE-SEM images of the pure PVDF and PVDF/KNN films, and the image of the KNN particles is given in Figure S4. The pure PVDF film has a continuous, gently undulating surface, consistent with spherulitic or lamellar domains formed during solvent evaporation. No cracks or phase separation are visible, indicating good film integrity. The PVDF/KNN film is rougher and more heterogeneous, with dispersed granular features attributed to embedded KNN particles. At the highest loading (0.5:0.5 g), particle clusters are visible (Figure S6), which is consistent with the agglomeration invoked in Section 3.4. These morphological changes are consistent with the electrical results discussed below.

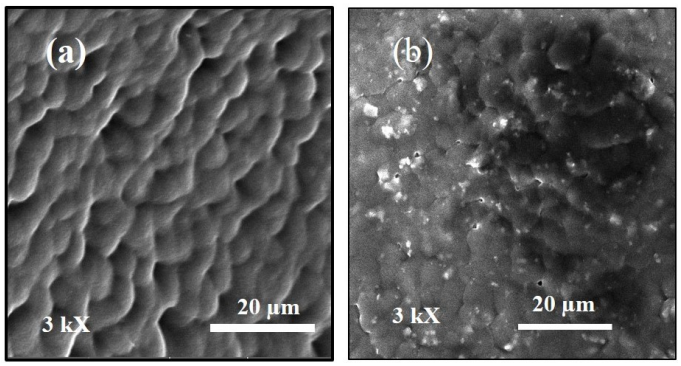



**Figure 3.** FE-SEM images of (a) pure PVDF and (b) a PVDF/KNN composite film.

### 3.3 FTIR analysis

Figure 4(a) shows the FTIR spectra of the PVDF and PVDF/KNN films. The bands at 471, 840, 1275 and 1431 cm$^{-1}$ are characteristic of the $\beta$-phase, whereas the band at 763 cm$^{-1}$ belongs to the $\alpha$-phase [30, 31]. As the KNN content increases, the 763 cm$^{-1}$ band weakens and is lowest at a PVDF:KNN mass ratio of 0.5:0.4. The $\beta$-phase fraction, $F(\beta)$, was calculated from the absorbance with Eq. (2), derived from the

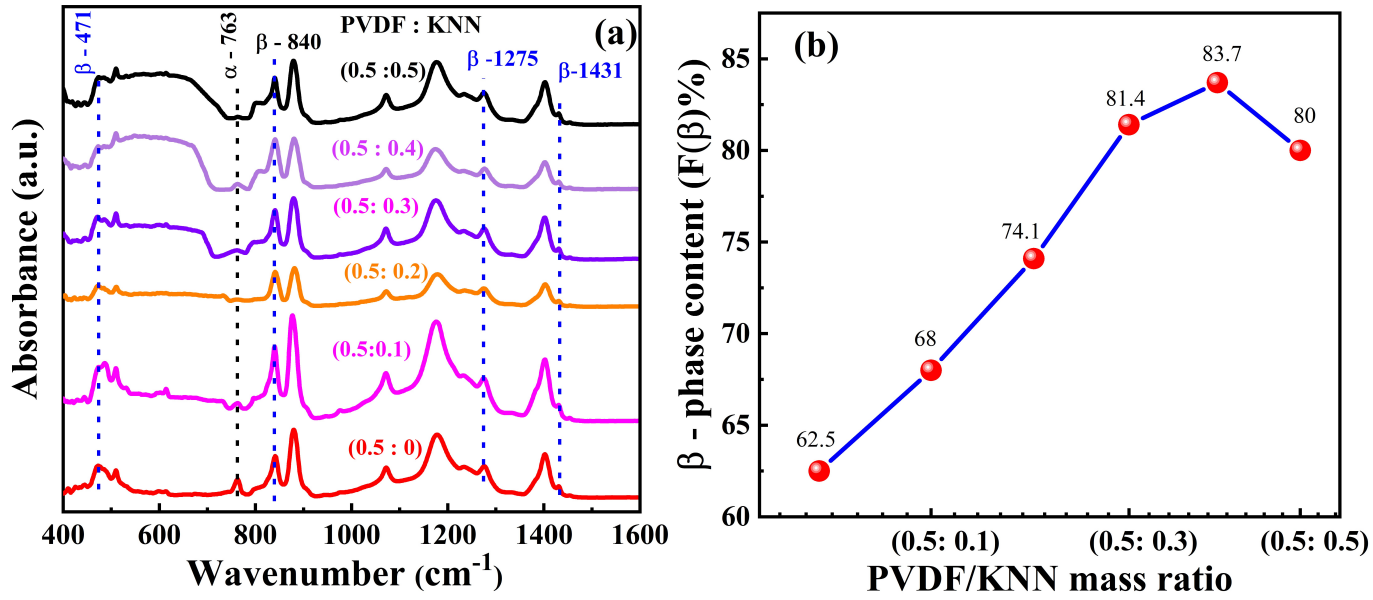



**Figure 4.** (a) FTIR spectra of pure PVDF and PVDF/KNN composite films with different KNN loadings; (b) $\beta$-phase fraction, $F(\beta)$, as a function of the PVDF:KNN mass ratio.

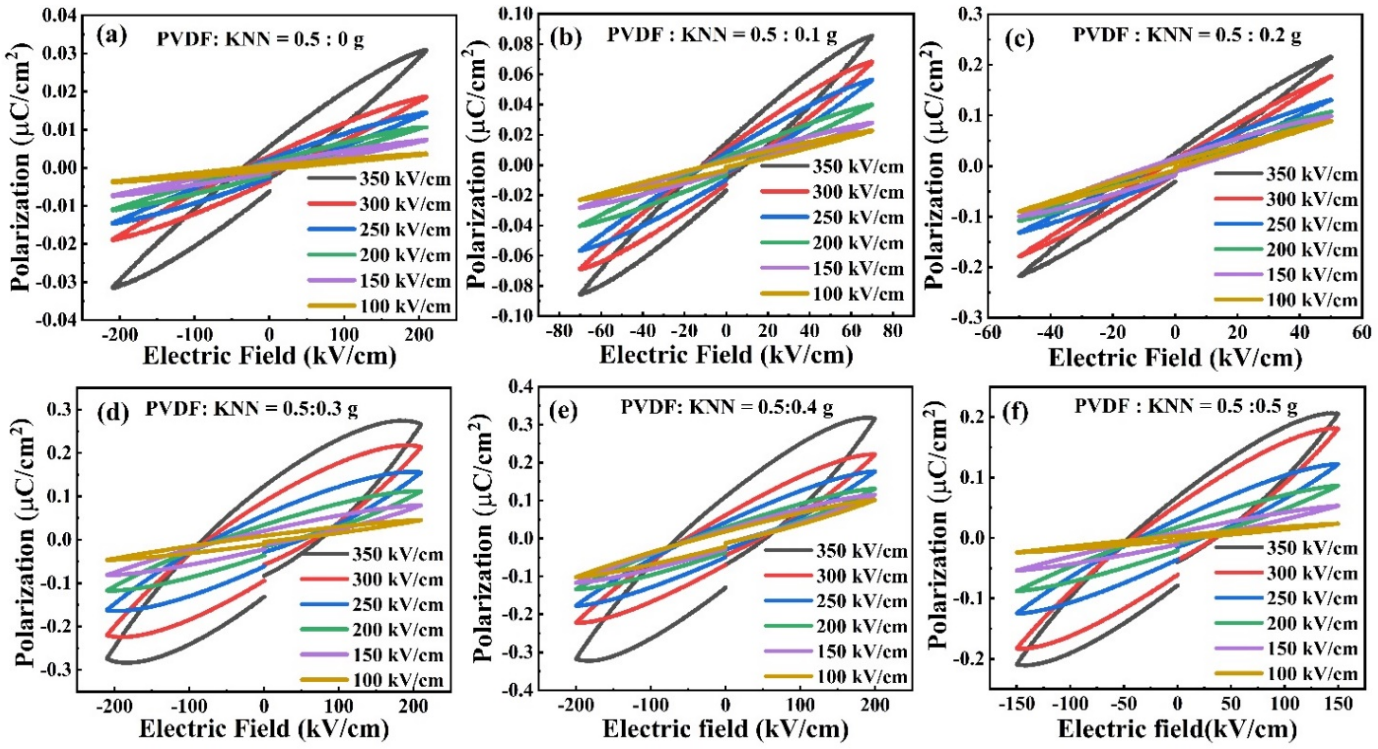



**Figure 5.** $P$-$E$ hysteresis loops of PVDF and PVDF/KNN composite films measured at 100-350 kV cm$^{-1}$: (a) 0.5:0 g (pure PVDF), (b) 0.5:0.1 g, (c) 0.5:0.2 g, (d) 0.5:0.3 g, (e) 0.5:0.4 g and (f) 0.5:0.5 g.

Beer-Lambert law [30]:

$$F(\beta) = \frac{A_\beta}{(K_\beta/K_\alpha)\,A_\alpha + A_\beta} \times 100\% = \frac{A_\beta}{1.26A_\alpha + A_\beta} \times 100\% \quad (2)$$

where $A_\alpha$ and $A_\beta$ are the absorbances of the $\alpha$- and $\beta$-phase bands at 763 and 840 cm$^{-1}$, and $K_\alpha$ ($6.1 \times 10^4$ cm$^2$ mol$^{-1}$) and $K_\beta$ ($7.7 \times 10^4$ cm$^2$ mol$^{-1}$) are the corresponding absorption coefficients.

As shown in Figure 4(b), $F(\beta)$ depends on the PVDF/KNN mass ratio. It rises from 62.5% for pure PVDF to 68%, 74.1%, 81.4% and 83.7% at 0.1, 0.2, 0.3 and 0.4 g KNN, and then falls to 80% at 0.5:0.5. A comparison with reported values is given in Table S1. The FTIR results agree with the XRD data. Because

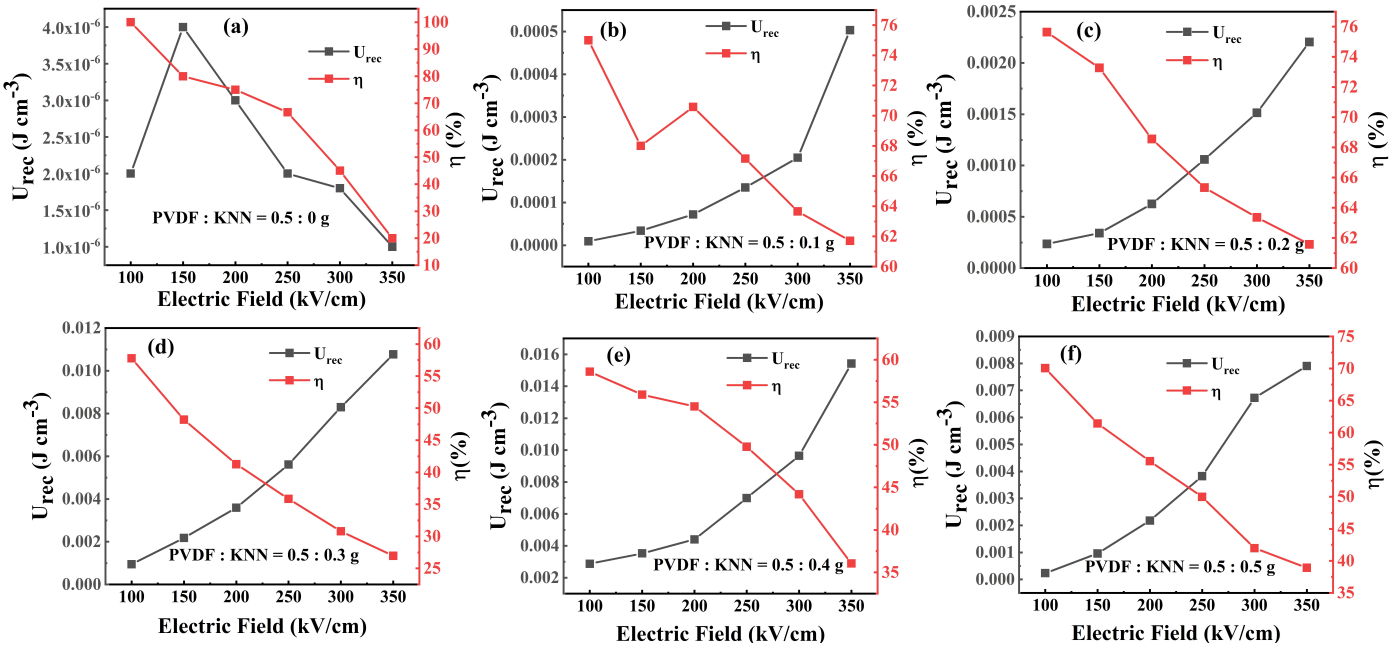



**Figure 6.** (a-f) Recoverable energy density ($U_{\mathrm{rec}}$) and energy efficiency ($\eta$) versus applied field for pure PVDF and PVDF/KNN composite films with different KNN loadings. The pure-PVDF data in (a) are not physically consistent (see Table S3, notes a-c) and are shown for completeness only.

the $\beta$-phase is polar, its higher content is expected to strengthen the ferroelectric response of the composites.

### 3.4 Ferroelectric analysis

The ferroelectric response of the PVDF and PVDF/KNN films was evaluated from $P$-$E$ loops recorded at applied fields of 100-350 kV cm$^{-1}$ (Figure 5(a-f)). The loops widen as the field increases, and the KNN filler clearly changes the response of the PVDF matrix. Pure PVDF gives a narrow loop with low polarization, whereas KNN addition increases both the polarization and the dipolar interaction. The higher $\beta$-phase content is expected to contribute to this improvement, and interfacial polarization at the PVDF/KNN boundaries may contribute as well.

The films containing 0.2-0.4 g KNN show the highest $P_{\mathrm{max}}$ values (0.213, 0.273 and 0.321 $\mu$C cm$^{-2}$, respectively), and the 0.4 g film gives the strongest response; the 0.3-0.5 g films also show the broadest loops. The $E_{\mathrm{c}}$, $P_{\mathrm{r}}$ and $P_{\mathrm{max}}$ values for all compositions and fields are listed in Table S2. Increasing the KNN loading to 0.5 g lowers $P_{\mathrm{max}}$ to 0.208 $\mu$C cm$^{-2}$, possibly because particle agglomeration restricts dipole mobility in the film.

The evolution of the loops with field shows a change in polarization behaviour. Up to 250 kV cm$^{-1}$ the loops are comparatively narrow ($P_{\mathrm{r}}/P_{\mathrm{max}} \leq 0.17$ for the 0-0.2 g films and 0.13-0.36 for the 0.3-0.5 g films; Table S2), but they are not linear, since every film already shows a finite $P_{\mathrm{r}}$ and $E_{\mathrm{c}}$. Above 250 kV cm$^{-1}$ the loops broaden further, indicating increased field-induced polarization and domain switching. A schematic of the linear-dielectric, relaxor-ferroelectric and high-entropy superparaelectric regimes is given in Figure S5. The polarization difference $\Delta P = P_{\mathrm{max}} - P_{\mathrm{r}}$ is a key indicator of energy-storage capability; the values at 350 kV cm$^{-1}$ are listed in Table 1. The 0.4 g film shows the highest $\Delta P$ (0.211 $\mu$C cm$^{-2}$) and $P_{\mathrm{max}}$ in the series.

Figure 6(a-f) shows $U_{\mathrm{rec}}$ and $\eta$ as functions of the applied field for all films. In every film, both quantities depend strongly on the field through the field-dependent polarization. $U_{\mathrm{rec}}$ was calculated from the $P$-$E$ loops by integrating the discharge branch, Eq. (3), as is done for PVDF-based composite films [26]:

$$U_{\mathrm{rec}} = \int_{P_{\mathrm{r}}}^{P_{\mathrm{max}}} E \, \mathrm{d}P \tag{3}$$

and $\eta$ was obtained from Eq. (4):

$$\eta = \frac{U_{\mathrm{rec}}}{U_{\mathrm{T}}} \times 100\% = \frac{U_{\mathrm{rec}}}{U_{\mathrm{rec}} + U_{\mathrm{loss}}} \times 100\% \tag{4}$$

where $U_{\mathrm{T}} = \int_0^{P_{\mathrm{max}}} E \, \mathrm{d}P$ is the total (charged) energy density and $U_{\mathrm{loss}}$ is the energy lost by hysteresis. Both integrals are taken over the first quadrant of the loop: $U_{\mathrm{T}}$ along the charging branch $E_{\mathrm{ch}}(P)$ ($E$ rising from 0 to $E_{\mathrm{max}}$) and $U_{\mathrm{rec}}$ along the discharging branch $E_{\mathrm{dis}}(P)$ ($E$ falling from $E_{\mathrm{max}}$ to 0, $P$ falling from $P_{\mathrm{max}}$ to

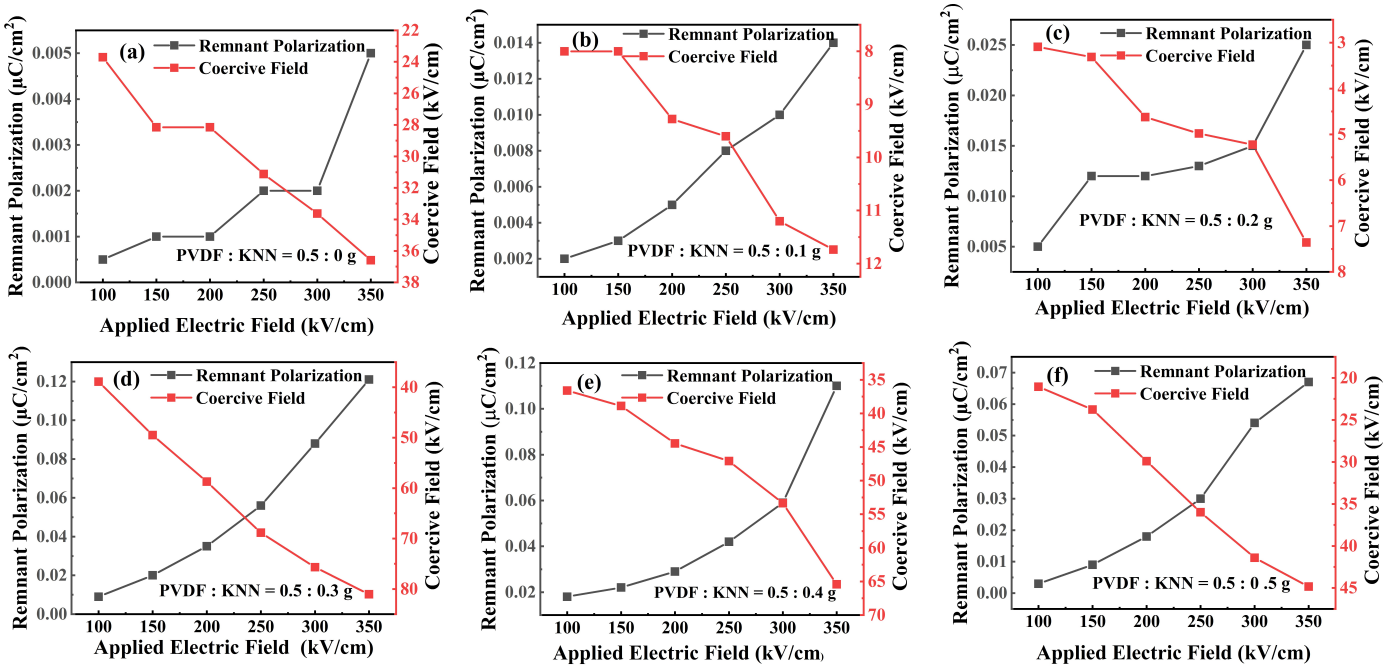



**Figure 7.** Variation of $P_r$ and $E_c$ with applied field for pure PVDF and PVDF/KNN composite films with different KNN loadings.

**Table 1.** Maximum polarization ($P_{max}$), remnant polarization ($P_r$) and polarization difference ($\Delta P$) of PVDF and PVDF/KNN composite films at 350 kV cm$^{-1}$ (films dried under a 3 kV DC voltage).

| PVDF:KNN (g) | $P_{max}$ ($\mu$C cm$^{-2}$) | $P_r$ ($\mu$C cm$^{-2}$) | $\Delta P$ ($\mu$C cm$^{-2}$) |
|---|---|---|---|
| 0.5:0 | 0.030 | 0.005 | 0.025 |
| 0.5:0.1 | 0.084 | 0.014 | 0.070 |
| 0.5:0.2 | 0.213 | 0.025 | 0.188 |
| 0.5:0.3 | 0.273 | 0.121 | 0.152 |
| 0.5:0.4 | 0.321 | 0.110 | 0.211 |
| 0.5:0.5 | 0.208 | 0.067 | 0.141 |

$P_r$). Hence $U_{loss} = U_T - U_{rec}$ is the area enclosed between the two branches and the $P$ axis. Because $0 \le E_{dis}(P) \le E_{ch}(P) \le E_{max}$ and $[P_r, P_{max}] \subseteq [0, P_{max}]$, any valid data set must satisfy

$$\begin{aligned} &0 \le U_{rec} \le E_{max}\Delta P, \\ &U_{rec} \le U_T \le E_{max}P_{max}, \\ &0 \le \eta \le 100\%, \end{aligned} \tag{5}$$

where 1 $\mu$C cm$^{-2}$ × 1 kV cm$^{-1}$ = 10$^{-3}$ J cm$^{-3}$. For a lossless linear dielectric, $U_T = U_{rec} = \frac{1}{2}E_{max}P_{max}$, which recovers Eq. (1). For the 0.3-0.5 g films all entries of Table S3 satisfy Eq. (5), with $U_T/(\frac{1}{2}E_{max}P_{max}) =$ 0.29-0.97, as expected for moderately hysteretic loops; for example, the 0.4 g film at 350 kV cm$^{-1}$ gives $U_{rec} = 0.0154 \le E_{max}\Delta P = 0.0739$ J cm$^{-3}$ and $U_T = 0.0428 \le E_{max}P_{max} = 0.112$ J cm$^{-3}$.

The energy values reported for pure PVDF are not physically consistent. At 200 and 150 kV cm$^{-1}$ the tabulated $U_{rec}$ exceeds $U_T$ (Table S3), which violates Eq. (5) and would correspond to $\eta = 107\%$ and 200%, i.e., more energy released than stored. In addition, all pure-PVDF values ($\le 5 \times 10^{-6}$ J cm$^{-3}$) are about three orders of magnitude below $\frac{1}{2}E_{max}P_{max}$ ($\approx 5 \times 10^{-3}$ J cm$^{-3}$ at 350 kV cm$^{-1}$), the value expected for its slim loop. The pure-PVDF energy data are therefore marked as invalid in Table S3 and Figure 6(a), are not used for any quantitative conclusion, and must be recalculated from the raw $P$-$E$ loops. Qualitatively, Table S2 shows that pure PVDF has by far the lowest $P_{max}$ and $\Delta P$ and hence the lowest storage capability. KNN addition improved the energy storage clearly. At 350 kV cm$^{-1}$, $U_{rec}$ rose from 0.000503 J cm$^{-3}$ for the 0.1 g film to 0.002205 J cm$^{-3}$ for the 0.2 g film, while $\eta$ changed only slightly (61.71% and 61.57%); these two films, however, also give $U_T$ values 10-90 times smaller than $\frac{1}{2}E_{max}P_{max}$ despite slim loops ($P_r/P_{max} \le 0.17$), so their absolute energy values require verification (see the note to Table S3). For the higher loadings, $U_{rec}$ increased steadily with field because of the larger

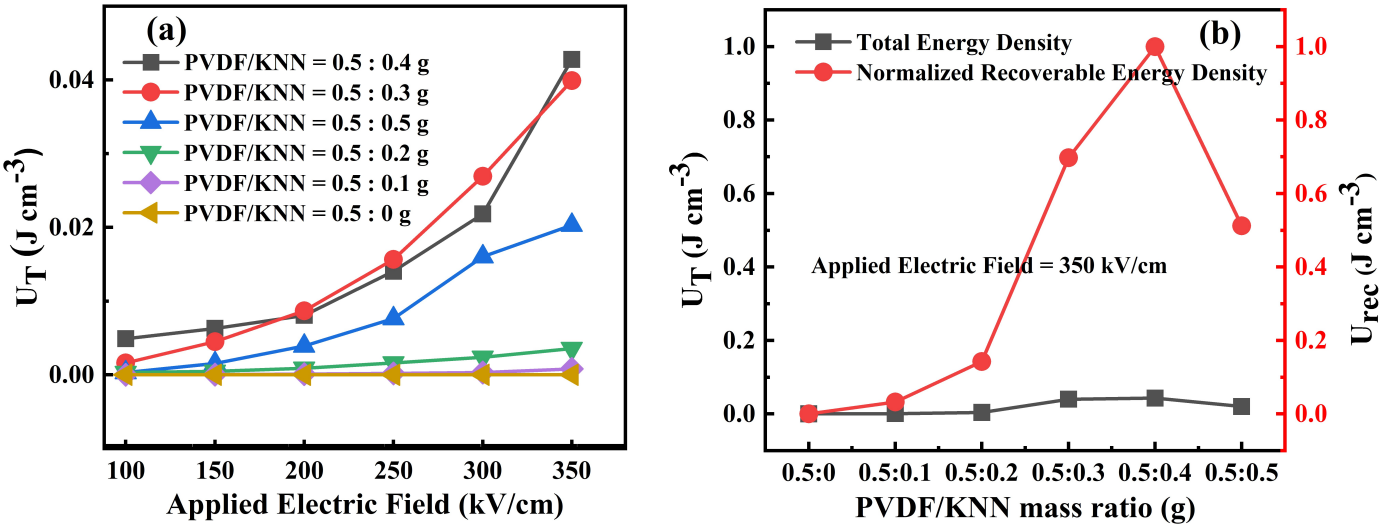



**Figure 8.** (a) Total energy density ($U_T$) versus applied field for pure PVDF and PVDF/KNN composite films; (b) $U_T$ (left axis) and $U_{rec}$ normalized to its maximum value (right axis, dimensionless) versus PVDF:KNN mass ratio at 350 kV cm$^{-1}$.

field-induced polarization. At 350 kV cm$^{-1}$, the 0.3, 0.4 and 0.5 g films reached $U_{rec}$ = 0.010764, 0.015428 and 0.007906 J cm$^{-3}$, with $\eta$ = 26.99%, 36.05% and 38.92% (Table S3). The 0.4 g film thus gives the highest $U_{rec}$ with an intermediate efficiency, i.e. the best compromise among the 0.3-0.5 g films.

Figure 7(a-f) shows $P_r$ and $E_c$ as functions of the applied field. For all compositions, $P_r$ increases with field, indicating better alignment of the dipolar domains. The magnitude of $E_c$ also rises with field in all films, which is consistent with more complete domain switching as the maximum field increases. For pure PVDF and the low-loading films (Figure 7(a-c)), $P_r$ and $E_c$ change in small, uneven steps (e.g. unchanged values between neighbouring fields), possibly because of interfacial polarization and local field fluctuations. At higher KNN loadings the variation is smoother, indicating stronger interfacial polarization and domain interaction.

Figures 8(a) and 8(b) show the energy storage as a function of field and of filler content, respectively. Figure 8(a) shows $U_T$ versus field. At low fields ($\leq$150 kV cm$^{-1}$) all films store little energy. $U_T$ rises sharply above ~250 kV cm$^{-1}$. The 0.5:0.4 g film gives the highest $U_T$ at 350 kV cm$^{-1}$ (0.04279 J cm$^{-3}$) and at $\leq$150 kV cm$^{-1}$. Between 200 and 300 kV cm$^{-1}$, however, the 0.5:0.3 g film shows a slightly higher $U_T$ (e.g. 0.026943 vs. 0.021824 J cm$^{-3}$ at 300 kV cm$^{-1}$), so the composition with the highest total energy density depends on the applied field. The larger $U_T$ of the 0.3 g film is not recovered: its $U_{rec}$ is lower than that of the 0.4 g film at every field, because its larger $P_r$ and broader loop raise $U_{loss}$ ($\eta$ = 30.79% vs. 44.18% at 300 kV cm$^{-1}$). In terms of the useful quantity, $U_{rec}$, the 0.4 g film is the best at all fields (Table S3), consistent with its highest $\beta$-phase fraction and $\Delta P$. The 0.1-0.2 g films give smaller $U_T$, in line with their lower $\beta$-phase content and $P_{max}$, and the 0.5 g film gives a lower $U_T$, possibly because of particle agglomeration. Figure 8(b) compares $U_T$ and $U_{rec}$ at 350 kV cm$^{-1}$: both increase with KNN content, peak at 0.5:0.4 g and then decrease. Note, however, that $\eta$ at this composition (36.05%) is lower than that of the 0.1-0.2 g films (≈62%), so the gain in stored energy is obtained at the cost of higher hysteresis loss. The $U_{rec}$ values are compared with literature data in Table 2. The present values

**Table 2.** Comparison of the recoverable energy density ($U_{rec}$) of this work with reported PVDF-based films (BT: $BaTiO_3$; BN: boron nitride; BST: $Ba_xSr_{1-x}TiO_3$).

| Filler / film | $U_{rec}$ (J cm$^{-3}$) | Ref. |
|---|---|---|
| $K_{0.5}Na_{0.5}NbO_3$-$SrTiO_3$/PVDF | 1.34 | [27] |
| Ca-substituted $Ba_{0.8}Sr_{0.2}TiO_3$/PVDF | 0.31 | [32] |
| BT-PVDF thick film | 9 | [33] |
| BN-BT/PVDF | 2.64 | [34] |
| BST/PVDF (0-3 type) | 11.61 | [35] |
| Pressed-and-folded $\beta$-PVDF film | 35 | [36] |
| PVDF/KNN film (0.5:0.4 g) | **0.0154** | **This work** |

are roughly 20 to 2000 times lower, mainly because the reported films were tested at much higher fields; raising the breakdown-limited test field is therefore the main direction for further work.

## 4 Conclusions

PVDF/KNN composite films were prepared by solvent casting with 0.5 g PVDF and 0.1-0.5 g KNN, and their structure, morphology and ferroelectric behaviour were studied. XRD and FTIR consistently showed that KNN addition increases the electroactive $\beta$-phase, and the 0.5:0.4 g film had the highest $\beta$-phase content (83.7%). In $P$-$E$ measurements at 100-350 kV cm$^{-1}$, the same composition gave $P_{\max} = 0.321$ $\mu$C cm$^{-2}$, $\Delta P = 0.211$ $\mu$C cm$^{-2}$, $U_{\text{rec}} \approx 0.0154$ J cm$^{-3}$, $\eta \approx 36.05\%$ and $U_{\text{T}} \approx 0.043$ J cm$^{-3}$ at 350 kV cm$^{-1}$; its $U_{\text{rec}}$ was the highest of the series at every field, whereas the 0.5:0.3 g film gave a slightly higher $U_{\text{T}}$ at 200-300 kV cm$^{-1}$ but with larger hysteresis loss. KNN therefore raises both the $\beta$-phase content and the ferroelectric response of PVDF. The 0.5:0.4 g composition is the optimum within this series and is a candidate lead-free flexible dielectric; its energy density must, however, be raised substantially, mainly through higher breakdown strength and lower hysteresis loss, before practical capacitor use.

## Data Availability Statement

The data that support the findings of this study are available from the corresponding authors upon reasonable request.

## Funding

The authors thank the Higher Education Commission (HEC), Islamabad, Pakistan for financial support under project Ref. No. 20-140245-75/NRPU/R&D/HEC/2026.

## Conflicts of Interest

The authors declare no conflicts of interest.

## AI Use Statement

The authors declare that no generative AI was used in the preparation of this manuscript.

## Ethical Approval and Consent to Participate

Not applicable. This study did not involve human participants or animals.

## References

[1] Nie, L., Fu, P., Cai, K., Deng, P., Bai, Y., Cai, C., ... & Guo, D. (2025). Tailoring the polyvinylidene fluoride phase structure in high permittivity MXene/polyvinylidene fluoride composite films via supercooling of the polymer melt. *Polymer Composites, 46*(10), 9634-9645. [CrossRef]

[2] Golriz, M., Moghari, S., Pourheidar, D., Othman, R. S., & Khonakdar, H. A. (2026). Dielectric, ferroelectric, and electric applications of polymers: recent advances and progress. *Polymers for Advanced Technologies, 37*(2), e70536. [CrossRef]

[3] Ali, N., Ali, A., Yousaf, J., Khan, S., Din, J. U., Shah, S. K., & Hayat, K. (2026). Strategies for $\beta$-phase enhancement in PVDF toward advanced flexible ferroelectric and piezoelectric devices. *Energy Technology, 14*(4), e202502400. [CrossRef]

[4] Wu, J. J., Li, D., Lai, Q., Bian, J., Zhang, A. P., Yang, S. K., ... & Chen, D. Q. (2026). Polyvinylidene Fluoride (PVDF)-Based Composite for Energy and Environmental Applications: A Comprehensive Review. *Polymer Composites, 47*(10), 8745-8775. [CrossRef]

[5] Bahuguna, A. S., & Panwar, V. (2026). A review on vital importance of beta phase in PVDF based carbon nanomaterial for sensing applications. *Discover Applied Sciences, 8*, 578. [CrossRef]

[6] Din, J. U., Khan, S., Shah, S. K., Ali, N., Yousaf, J., Ahmed, E., ... & Hayat, K. (2026). Electrospun PVDF/BaTiO3 composite nanofibers with enhanced $\beta$-phase for flexible piezoelectric nanogenerator applications. *Journal of Materials Science: Materials in Electronics, 37*(15), 1156. [CrossRef]

[7] Athira, B. S., George, A., Vaishna Priya, K., Hareesh, U. S., Gowd, E. B., Surendran, K. P., & Chandran, A. (2022). High-performance flexible piezoelectric nanogenerator based on electrospun PVDF-$BaTiO_3$ nanofibers for self-powered vibration sensing applications. *ACS Applied Materials & Interfaces, 14*(39), 44239-44250. [CrossRef]

[8] Yousaf, J., Hayat, K., Khan, S., Din, J. U., Ali, N., Ali, S., Khan, Y., & Shah, S. K. (2025). $Ti_3C_2$-MXene/ZnO/PVDF composite fibers as renewable energy materials for piezoelectric nanogenerator applications. *Journal of Alloys and Compounds, 1039*, 183392. [CrossRef]

[9] El-Aassar, M. R., Hassan, H. M. A., & Essawy, A. A. (2026). Development of PVDF@ZnO hybrid nanofibers with improved $\beta$-phase crystallinity and photocatalytic efficiency. *Inorganic Chemistry Communications, 188*, 116558. [CrossRef]

[10] Kaplan, M., Alp, E., Borazan, I., Krause, B., & Pötschke, P. (2025). Enhanced piezoelectric performance of poly (vinylidene fluoride) nanocomposites with synthesized zinc oxide nanowires and branched carbon nanotubes via melt mixing

process. *Macromolecular Materials and Engineering, 310*(9), e00122. [CrossRef]

[11] Lopes, A. C., Costa, C. M., Tavares, C. J., Neves, I. C., & Lanceros-Mendez, S. (2011). Nucleation of the electroactive $\gamma$ phase and enhancement of the optical transparency in low filler content poly (vinylidene)/clay nanocomposites. *The Journal of Physical Chemistry C, 115*(37), 18076-18082. [CrossRef]

[12] Sukumaran, S., Szewczyk, P. K., & Stachewicz, U. (2026). Triboelectric Performance of Electrospun PVDF Fibers for Energy Harvesting: A Comparative Study of Boron Nitride (BN) and Reduced Graphene Oxide (rGO) Fillers. *Materials, 19*(3), 475. [CrossRef]

[13] Zhang, L., Li, S., Zhu, Z., Rui, G., Du, B., Chen, D., ... & Zhu, L. (2023). Recent progress on structure manipulation of poly (vinylidene fluoride)-based ferroelectric polymers for enhanced piezoelectricity and applications. *Advanced Functional Materials, 33*(38), 2301302. [CrossRef]

[14] Huang, Y., Rui, G., Li, Q., Allahyarov, E., Li, R., Fukuto, M., ... & Zhu, L. (2021). Enhanced piezoelectricity from highly polarizable oriented amorphous fractions in biaxially oriented poly (vinylidene fluoride) with pure $\beta$ crystals. *Nature communications, 12*(1), 675. [CrossRef]

[15] Chen, X., Qin, H., Qian, X., Zhu, W., Li, B., Zhang, B., ... & Zhang, Q. M. (2022). Relaxor ferroelectric polymer exhibits ultrahigh electromechanical coupling at low electric field. *Science, 375*(6587), 1418-1422. [CrossRef]

[16] Zhu, Z., Rui, G., Li, Q., Allahyarov, E., Li, R., Soulestin, T., ... & Zhu, L. (2021). Electrostriction-enhanced giant piezoelectricity via relaxor-like secondary crystals in extended-chain ferroelectric polymers. *Matter, 4*(11), 3696-3709. [CrossRef]

[17] Chang, J., Dommer, M., Chang, C., & Lin, L. (2012). Piezoelectric nanofibers for energy scavenging applications. *Nano energy, 1*(3), 356-371. [CrossRef]

[18] Cao, W., Li, T., Chen, P., & Wang, C. (2021). Outstanding energy storage performance of $Na_{0.5}Bi_{0.5}TiO_3$-$BaTiO_3$-$(Sr_{0.85}Bi_{0.1})(Mg_{1/3}Nb_{2/3})O_3$ lead-free ceramics. *ACS Applied Energy Materials, 4*(9), 9362-9367. [CrossRef]

[19] Lu, Z., Wang, G., Bao, W., Li, J., Li, L., Mostaed, A., ... & Reaney, I. M. (2020). Superior energy density through tailored dopant strategies in multilayer ceramic capacitors. *Energy & Environmental Science, 13*(9), 2938-2948. [CrossRef]

[20] Zhang, H., Wei, T., Zhang, Q., Ma, W., Fan, P., Salamon, D., ... & Ye, Z. G. (2020). A review on the development of lead-free ferroelectric energy-storage ceramics and multilayer capacitors. *Journal of Materials Chemistry C, 8*(47), 16648-16667. [CrossRef]

[21] Yang, Z., Gao, F., Du, H., Jin, L., Yan, L., Hu, Q., ... & Wang, Y. J. (2019). Grain size engineered lead-free ceramics with both large energy storage density and ultrahigh mechanical properties. *Nano Energy, 58*, 768-777. [CrossRef]

[22] Hu, Q., Tian, Y., Zhu, Q., Bian, J., Jin, L., Du, H., ... & Wei, X. (2020). Achieve ultrahigh energy storage performance in $BaTiO_3$-$Bi(Mg_{1/2}Ti_{1/2})O_3$ relaxor ferroelectric ceramics via nano-scale polarization mismatch and reconstruction. *Nano Energy*, 67, 104264. [CrossRef]

[23] Prateek, N., Thakur, V. K., & Gupta, R. K. (2016). Recent progress on ferroelectric polymer-based nanocomposites for high energy density capacitors: synthesis, dielectric properties, and future aspects. *Chemical reviews, 116*(7), 4260-4317. [CrossRef]

[24] Tripathy, A., Maria Joseph Raj, N. P., Kim, S. J., & Ramadoss, A. (2023). Elucidating the piezoelectric, ferroelectric, and dielectric performance of lead-free KNN/PVDF and its copolymer-based flexible composite films. *ACS Applied Electronic Materials, 5*(10), 5422-5431. [CrossRef]

[25] Hai, Q., Ren, F., Zhong, P., Dou, X., Li, J., & Mao, J. (2026). Molecular Engineering of DAP Grafted Polypropylene for Ultrahigh-Energy-Density Film Capacitors and Smart Electrostatic Adhesion. *Advanced Functional Materials, 36*(16), e20883. [CrossRef]

[26] Wang, L., Zhang, Y., Li, S., Yao, Z., Hao, H., Cao, M., ... & Liu, H. (2026). Trace BaTiO3 Doping-Derived PVDF-Based Composite Thick Film for Dielectric Energy Storage. *Materials, 19*(6), 1137. [CrossRef]

[27] Chen, C., Wang, L., Liu, X., Yang, W., Lin, J., Chen, G., & Yang, X. (2019). $K_{0.5}Na_{0.5}NbO_3$-$SrTiO_3$/PVDF polymer composite film with low remnant polarization and high discharge energy storage density. *Polymers, 11*(2), 310. [CrossRef]

[28] Yang, L., Kong, X., Li, F., Hao, H., Cheng, Z., Liu, H., ... & Zhang, S. (2019). Perovskite lead-free dielectrics for energy storage applications. *Progress in Materials Science, 102*, 72-108. [CrossRef]

[29] Martins, P., Lopes, A. C., & Lanceros-Mendez, S. (2014). Electroactive phases of poly (vinylidene fluoride): Determination, processing and applications. *Progress in polymer science, 39*(4), 683-706. [CrossRef]

[30] Gregorio, Jr, R., & Cestari, M. (1994). Effect of crystallization temperature on the crystalline phase content and morphology of poly (vinylidene fluoride). *Journal of Polymer Science Part B: Polymer Physics, 32*(5), 859-870. [CrossRef]

[31] Cai, X., Lei, T., Sun, D., & Lin, L. (2017). A critical analysis of the $\alpha$, $\beta$ and $\gamma$ phases in poly(vinylidene fluoride) using FTIR. *RSC Advances, 7*(25), 15382-15389. [CrossRef]

[32] Jena, L. K., Chahal, S., Sahoo, S., Boomishankar, R., & Asthana, S. (2025). Energy storage and harvesting potential of eco-friendly Ca-substituted $Ba_{0.8}Sr_{0.2}TiO_3$/PVDF ferro-flexible composite films. *ACS Applied Electronic Materials, 7*(3), 1314-1328. [CrossRef]

[33] Ait Laasri, H., Fasquelle, D., Tachafine, A., Carru, J. C., Rguiti, M., & Elaatmani, M. (2021). Ferroelectric BT–PVDF Composite Thick Films for Electrical Energy Storage. *Journal of Electronic Materials, 50*(3), 1132-1139. [CrossRef]

[34] Guan, L., Zhao, X., Ji, Z., Jiang, M., Cui, Y., Weng, L., ... & Liu, J. (2023). Preparation of 3D BN-BT/PVDF skeleton structure composites for high thermal conductivity and energy storage. *Polymer Testing, 125*, 108126. [CrossRef]

[35] Tong, Y., Lai, J., Tian, Y., Liu, J., Pei, W., Yong, H., ... & Hu, J. (2025). Dielectric energy storage properties of 0–3 type BST/PVDF composite films. *Ceramics International, 51*(7), 8362-8375. [CrossRef]

[36] Meng, N., Ren, X., Santagiuliana, G., Ventura, L., Zhang, H., Wu, J., Yan, H., Reece, M. J., & Bilotti, E. (2019). Ultrahigh $\beta$-phase content poly(vinylidene fluoride) with relaxor-like ferroelectricity for high energy density capacitors. *Nature Communications, 10*, 4535. [CrossRef]

[37] Kumar, R. N., & Hemalatha, J. (2025). Preparation and characterization of PVDF/$CoFe_2O_4$/g-$C_3N_4$ nanocomposite films for multi-functional applications. *Journal of Magnetism and Magnetic Materials, 624*, 173029. [CrossRef]

[38] Liu, Q., Yu, H., Guan, M., Zhi, X., & Qin, S. (2025). Enhanced Dielectric Response in Poly (Vinylidene Fluoride) (PVDF) Ferroelectric Films via Zinc-Based Metal-Organic Complex. *Journal of Applied Polymer Science, 142*(47), e57863. [CrossRef]

[39] Nayak, B., Anwar, S., & Anwar, S. (2026). Free-standing PVDF film for piezoelectric energy harvesting and sensing applications. *Materials Science and Engineering: B, 323*, 118777. [CrossRef]

[40] Zain Karimy, N. H., Li, H., Lee, H. B., Ojha, D. P., Ovhal, M. M., Devaraj, V., ... & Kang, J. W. (2025). Highly Efficient 3D-Printed PVDF-Based Triboelectric Nanogenerators Featuring Polymorphic Perovskite Nanofillers. *Advanced Functional Materials, 35*(39), 2424271. [CrossRef]

## Supplementary Information

This appendix contains Figures S1-S6 and Tables S1-S3 cited in the main text.

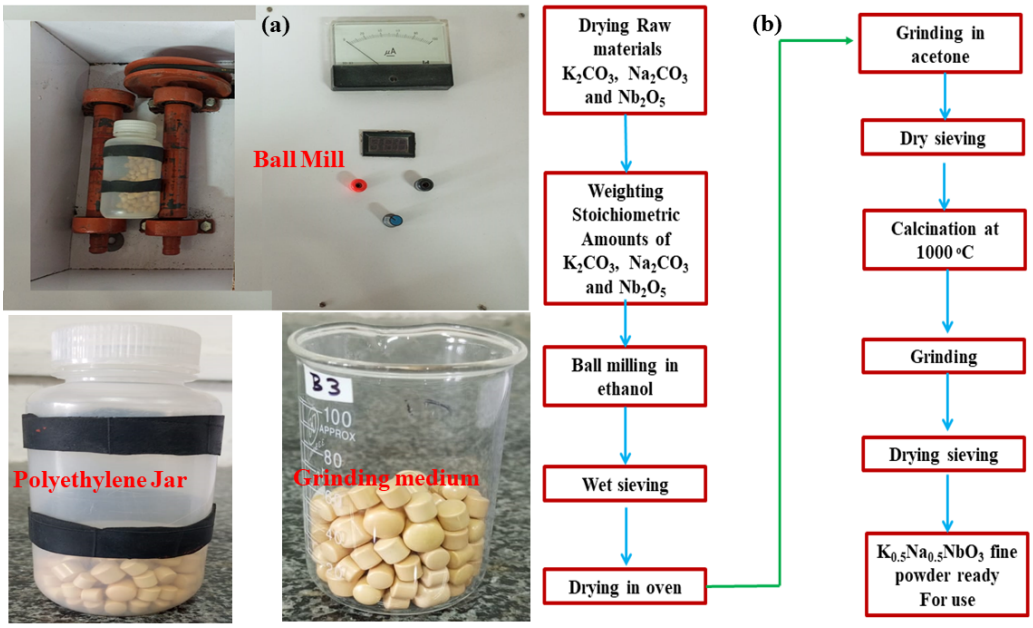



**Figure S1.** (a) Equipment used for KNN powder synthesis (ball mill, polyethylene milling jar and grinding media). (b) Flow diagram of the solid-state reaction route used to synthesize $K_{0.5}Na_{0.5}NbO_3$ (KNN) powder.




**Figure S2.** As-prepared PVDF/KNN composite films with different KNN loadings, prepared by solvent casting and dried at 80 °C under a 3 kV DC voltage before ferroelectric testing.

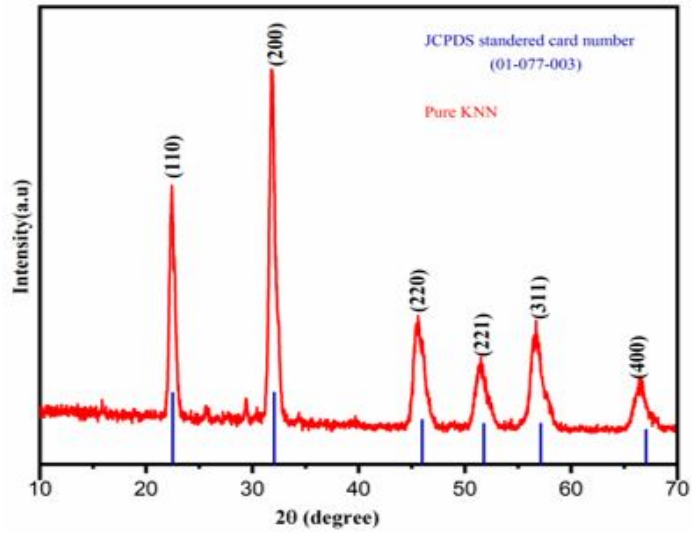



**Figure S3.** XRD pattern of the synthesized KNN powder.

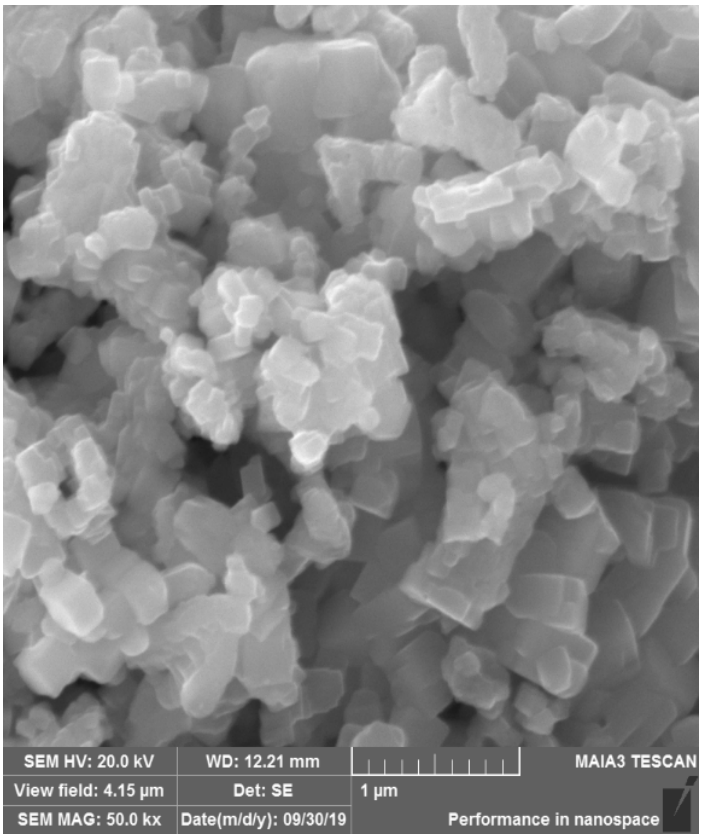



**Figure S4.** FE-SEM image of the synthesized KNN powder.

**Table S1.** Comparison of the electroactive $\beta$-phase content of this work with recently reported values.

| No. | Composition | $\beta$-phase content (%) | Ref. |
|---|---|---|---|
| 1 | PVDF/$CoFe_2O_4$/g-$C_3N_4$ composite film | 51 | [37] |
| 2 | SAZn/PVDF composite film | 74.8 | [38] |
| 3 | PVDF film | 69.25 | [39] |
| 4 | PVDF/$FAPbI_3$ composite film | 83 | [40] |
| 5 | KNN/PVDF composite film | 85 | [24] |
| 6 | PVDF/KNN composite film (0.5:0.4 g) | 83.7 | This work |

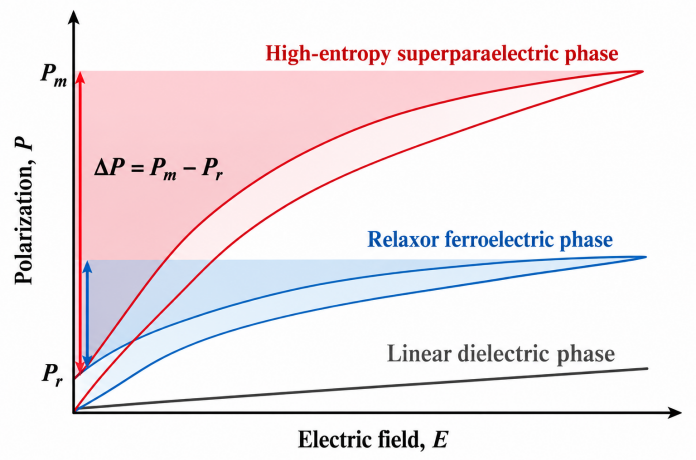



**Figure S5.** Schematic of energy storage in dielectric materials: $P$-$E$ loops of linear dielectric, relaxor-ferroelectric and high-entropy superparaelectric materials. Shaded areas indicate $U_{\mathrm{rec}}$; arrows indicate $\Delta P = P_{\mathrm{max}} - P_{\mathrm{r}}$ (labelled $P_{\mathrm{m}}$ and $P_{\mathrm{r}}$ in the schematic).

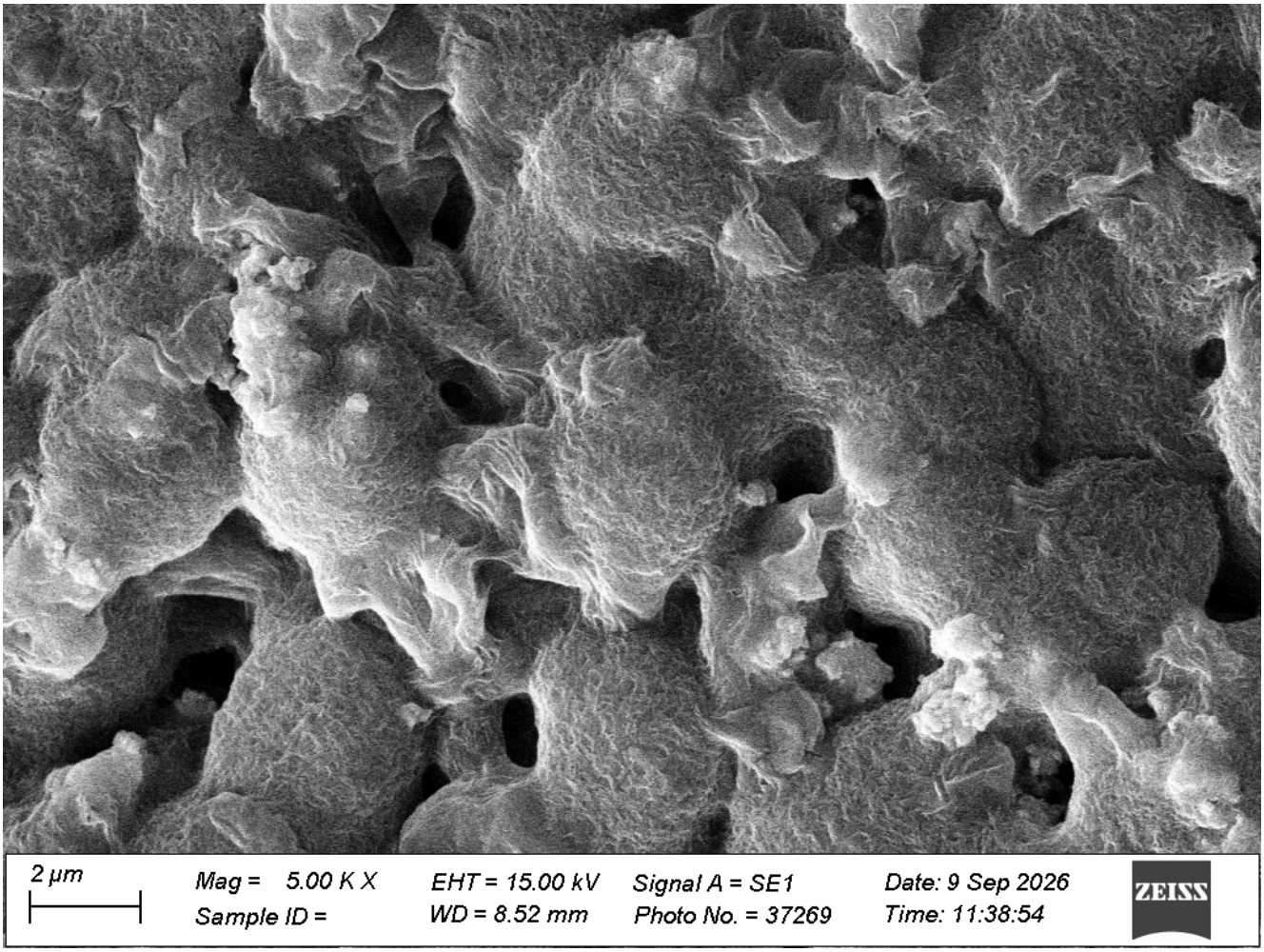



**Figure S6.** FE-SEM image of the PVDF/KNN composite film (0.5:0.5 g).

**Table S2.** Maximum polarization ($P_{max}$), remnant polarization ($P_r$) and coercive field ($E_c$) at each applied field for PVDF and PVDF/KNN composite films (dried under a 3 kV DC voltage).

| PVDF:KNN (g) | $E$ (kV cm$^{-1}$) | $P_{max}$ ($\mu$C cm$^{-2}$) | $P_r$ ($\mu$C cm$^{-2}$) | $E_c$ (kV cm$^{-1}$) |
|---|---|---|---|---|
| 0.5:0 (pure PVDF) | 350 | 0.030 | 0.005 | −36.593 |
| 0.5:0 (pure PVDF) | 300 | 0.018 | 0.002 | −33.629 |
| 0.5:0 (pure PVDF) | 250 | 0.014 | 0.002 | −31.121 |
| 0.5:0 (pure PVDF) | 200 | 0.010 | 0.001 | −28.157 |
| 0.5:0 (pure PVDF) | 150 | 0.007 | 0.001 | −28.157 |
| 0.5:0 (pure PVDF) | 100 | 0.003 | 0.0005 | −23.711 |
| 0.5:0.1 | 350 | 0.084 | 0.014 | −11.737 |
| 0.5:0.1 | 300 | 0.068 | 0.010 | −11.203 |
| 0.5:0.1 | 250 | 0.056 | 0.008 | −9.603 |
| 0.5:0.1 | 200 | 0.039 | 0.005 | −9.275 |
| 0.5:0.1 | 150 | 0.027 | 0.003 | −8.002 |
| 0.5:0.1 | 100 | 0.022 | 0.002 | −8.002 |
| 0.5:0.2 | 350 | 0.213 | 0.025 | −7.359 |
| 0.5:0.2 | 300 | 0.175 | 0.015 | −5.225 |
| 0.5:0.2 | 250 | 0.131 | 0.013 | −4.979 |
| 0.5:0.2 | 200 | 0.107 | 0.012 | −4.623 |
| 0.5:0.2 | 150 | 0.098 | 0.012 | −3.310 |
| 0.5:0.2 | 100 | 0.088 | 0.005 | −3.091 |
| 0.5:0.3 | 350 | 0.273 | 0.121 | −81.053 |
| 0.5:0.3 | 300 | 0.215 | 0.088 | −75.695 |
| 0.5:0.3 | 250 | 0.157 | 0.056 | −68.855 |
| 0.5:0.3 | 200 | 0.113 | 0.035 | −58.709 |
| 0.5:0.3 | 150 | 0.079 | 0.020 | −49.475 |
| 0.5:0.3 | 100 | 0.045 | 0.009 | −38.874 |
| 0.5:0.4 | 350 | 0.321 | 0.110 | −65.435 |
| 0.5:0.4 | 300 | 0.223 | 0.059 | −53.351 |
| 0.5:0.4 | 250 | 0.176 | 0.042 | −47.081 |
| 0.5:0.4 | 200 | 0.131 | 0.029 | −44.459 |
| 0.5:0.4 | 150 | 0.114 | 0.022 | −38.874 |
| 0.5:0.4 | 100 | 0.101 | 0.018 | −36.593 |
| 0.5:0.5 | 350 | 0.208 | 0.067 | −44.847 |
| 0.5:0.5 | 300 | 0.183 | 0.054 | −41.415 |
| 0.5:0.5 | 250 | 0.122 | 0.030 | −35.989 |
| 0.5:0.5 | 200 | 0.086 | 0.018 | −29.925 |
| 0.5:0.5 | 150 | 0.053 | 0.009 | −23.780 |
| 0.5:0.5 | 100 | 0.023 | 0.003 | −21.067 |

**Table S3.** Total energy density ($U_{\mathrm{T}}$), recoverable energy density ($U_{\mathrm{rec}}$) and efficiency ($\eta$) of PVDF and PVDF/KNN composite films (dried under a 3 kV DC voltage).

| PVDF:KNN (g) | $E$ (kV cm$^{-1}$) | $U_{\mathrm{T}}$ (J cm$^{-3}$) | $U_{\mathrm{rec}}$ (J cm$^{-3}$) | $\eta$ (%) |
|---|---|---|---|---|
| 0.5:0 (pure PVDF)[a] | 350 | 0.000005 | 0.000001 | 20 |
| 0.5:0 (pure PVDF)[a] | 300 | 0.000004 | 0.0000018 | 45 |
| 0.5:0 (pure PVDF)[a] | 250 | 0.000003 | 0.000002 | 66.66 |
| 0.5:0 (pure PVDF)[a,b] | 200 | 0.0000028 | 0.000003 | 75 |
| 0.5:0 (pure PVDF)[a,b] | 150 | 0.000002 | 0.000004 | 80 |
| 0.5:0 (pure PVDF)[a,c] | 100 | 0.000002 | 0.000002 | 100 |
| 0.5:0.1[d] | 350 | 0.000815 | 0.000503 | 61.71 |
| 0.5:0.1[d] | 300 | 0.000322 | 0.000205 | 63.66 |
| 0.5:0.1[d] | 250 | 0.000201 | 0.000135 | 67.16 |
| 0.5:0.1[d] | 200 | 0.000102 | 0.000072 | 70.58 |
| 0.5:0.1[d] | 150 | 0.00005 | 0.000034 | 68 |
| 0.5:0.1[d] | 100 | 0.000012 | 0.000009 | 75 |
| 0.5:0.2[d] | 350 | 0.003581 | 0.002205 | 61.57 |
| 0.5:0.2[d] | 300 | 0.00239 | 0.001514 | 63.36 |
| 0.5:0.2[d] | 250 | 0.001621 | 0.001059 | 65.33 |
| 0.5:0.2[d] | 200 | 0.000913 | 0.000626 | 68.56 |
| 0.5:0.2[d] | 150 | 0.000464 | 0.00034 | 73.27 |
| 0.5:0.2[d] | 100 | 0.000312 | 0.000236 | 75.64 |
| 0.5:0.3 | 350 | 0.039886 | 0.010764 | 26.99 |
| 0.5:0.3 | 300 | 0.026943 | 0.008296 | 30.79 |
| 0.5:0.3 | 250 | 0.015647 | 0.00561 | 35.85 |
| 0.5:0.3 | 200 | 0.008695 | 0.003588 | 41.26 |
| 0.5:0.3 | 150 | 0.004517 | 0.002178 | 48.21 |
| 0.5:0.3 | 100 | 0.001636 | 0.000945 | 57.76 |
| 0.5:0.4 | 350 | 0.04279 | 0.015428 | 36.05 |
| 0.5:0.4 | 300 | 0.021824 | 0.009643 | 44.18 |
| 0.5:0.4 | 250 | 0.014056 | 0.006997 | 49.77 |
| 0.5:0.4 | 200 | 0.008065 | 0.004397 | 54.51 |
| 0.5:0.4 | 150 | 0.006304 | 0.003524 | 55.90 |
| 0.5:0.4 | 100 | 0.004901 | 0.002872 | 58.60 |
| 0.5:0.5 | 350 | 0.02031 | 0.007906 | 38.92 |
| 0.5:0.5 | 300 | 0.016024 | 0.006727 | 41.98 |
| 0.5:0.5 | 250 | 0.007649 | 0.003823 | 49.98 |
| 0.5:0.5 | 200 | 0.003917 | 0.002176 | 55.55 |
| 0.5:0.5 | 150 | 0.001563 | 0.00096 | 61.42 |
| 0.5:0.5 | 100 | 0.000334 | 0.000234 | 70.05 |

[a] The pure-PVDF energy values are about three orders of magnitude below $\frac{1}{2}E_{\max}P_{\max}$, are not physically consistent, and are not used for any quantitative conclusion; they must be recalculated from the raw $P$-$E$ loops.
[b] $U_{\mathrm{rec}} > U_{\mathrm{T}}$, which violates Eq. (5); the ratio $U_{\mathrm{rec}}/U_{\mathrm{T}}$ would be 107% at 200 kV cm$^{-1}$ and 200% at 150 kV cm$^{-1}$, and the tabulated $\eta$ (75% and 80%) does not match it.
[c] $U_{\mathrm{rec}} = U_{\mathrm{T}}$ ($\eta = 100\%$) would mean zero hysteresis loss, which is not physical for a ferroelectric polymer film.
[d] $U_{\mathrm{T}}$ is 10-90 times smaller than $\frac{1}{2}E_{\max}P_{\max}$ despite slim loops ($P_{\mathrm{r}}/P_{\max} \leq 0.17$); the absolute values require verification.

**Numan Ali** received the B.S. degree in physics from Abdul Wali Khan University Mardan (AWKUM), Pakistan, in 2020, and the M.Phil. degree in physics from the same university in 2023. His M.Phil. research focused on materials science, particularly the development of materials for nanogenerator applications. (Email: numanphysics435@gmail.com)

**Khizar Hayat** is a Professor of Physics at Abdul Wali Khan University Mardan, Khyber Pakhtunkhwa, Pakistan. He received the Ph.D. degree from PIEAS, Islamabad, in 2014, and completed postdoctoral research in China in 2018. His research interests include condensed matter physics, nanomaterials and optoelectronic devices. (Email: khizar3@awkum.edu.pk)

**Muhammad Uzair** is currently pursuing the Ph.D. degree in materials science at Abdul Wali Khan University Mardan (AWKUM), where he also received the B.S. and M.Phil. degrees in physics. His M.Phil. research focused on materials for energy conversion and storage devices. (Email: uzairkhanawkum11@gmail.com)

**Aisha Khattak** is currently pursuing the M.Phil. degree in materials science at Abdul Wali Khan University Mardan (AWKUM). Her M.Phil. research focuses on materials for energy conversion and storage devices. (Email: aishakhattak091@gmail.com)

**Said Karim Shah** is a Professor of Physics at Abdul Wali Khan University Mardan, Khyber Pakhtunkhwa, Pakistan. He received the Ph.D. degree from the University of Camerino, Italy, in 2012, and completed postdoctoral research at the Institut Polytechnique de Bordeaux, France, in 2014. His research interests include $TiO_2$ and ZnO nanostructures, solar cells, and organic-inorganic semiconductor devices. (Email: saidkarim@awkum.edu.pk)